

# Machine learning for predicting the $B_z$ magnetic field component from upstream in situ observations of solar coronal mass ejections

M. A. Reiss<sup>1</sup>, C. Möstl<sup>1</sup>, R. L. Bailey<sup>2</sup>, H. T. Rüdiger<sup>3,4</sup>, U. V. Amerstorfer<sup>1</sup>,  
T. Amerstorfer<sup>1</sup>, A. J. Weiss<sup>1,4</sup>, J. Hinterreiter<sup>1,4</sup>, and A. Windisch<sup>3,5,6</sup>

<sup>1</sup>Space Research Institute, Austrian Academy of Sciences, Schmiedlstraße 6, 8042 Graz, Austria

<sup>2</sup>Zentralanstalt für Meteorologie und Geodynamik, Hohe Warte 38, 1190 Vienna, Austria

<sup>3</sup>Know-Center GmbH, Inffeldgasse 13, 8010 Graz, Austria

<sup>4</sup>Institute of Physics, University of Graz, Universitätsplatz 5, 8010 Graz, Austria

<sup>5</sup>Department of Physics, Washington University in St. Louis, MO 63130, USA

<sup>6</sup>RL Community, AI AUSTRIA, Wollzeile 24/12, 1010 Vienna, Austria

## Key Points:

- We hypothesize that upstream in situ measurements are sufficient to predict the minimum value of the  $B_z$  component in solar coronal mass ejections.
- We present a predictive tool that forecasts the minimum of  $B_z$  in an ICME with a MAE of 3.12 nT and a PCC of 0.71.

arXiv:2108.04067v2 [physics.space-ph] 5 Nov 2021

**Abstract**

Predicting the  $B_z$  magnetic field embedded within ICMEs, also known as the  $B_z$  problem, is a key challenge in space weather forecasting. We study the hypothesis that upstream in situ measurements of the sheath region and the first few hours of the magnetic obstacle provide sufficient information for predicting the downstream  $B_z$  component.

To do so, we develop a predictive tool based on machine learning that is trained and tested on 348 ICMEs from Wind, STEREO-A, and STEREO-B measurements. We train the machine learning models to predict the minimum value of the  $B_z$  component and the maximum value of the total magnetic field  $B_t$  in the magnetic obstacle. To validate the tool, we let the ICMEs sweep over the spacecraft and assess how continually feeding in situ measurements into the tool improves the  $B_z$  prediction.

We specifically find that the predictive tool can predict the minimum value of the  $B_z$  component in the magnetic obstacle with a mean absolute error of 3.12 nT and a Pearson correlation coefficient of 0.71 when the sheath region and the first 4 hours of the magnetic obstacle are observed. While the underlying hypothesis is unlikely to solve the  $B_z$  problem, the tool shows promise for ICMEs that have a recognizable magnetic flux rope signature. Transitioning the tool to operations could lead to improved space weather forecasting.

**Plain Language Summary**

At any time, our solar system is populated with interplanetary coronal mass ejections (ICMEs). Solar scientists and space weather forecasters track ICMEs when they are ejected from the Sun and follow their path into the vast reaches of interplanetary space. They do so because if an ICME hits Earth, it could damage our infrastructure such as power-grids and GPS satellites, which are a mainstay of our modern civilization. The possible damage is primarily determined by the magnetic field embedded within the ICME. The North-South magnetic field component,  $B_z$ , plays a decisive role, especially if it is pointing opposite to Earth's magnetic field. Currently we cannot predict  $B_z$  with sufficient accuracy. Scientists often refer to our limited predictive abilities as the  $B_z$  problem. Here we shine a new light on the  $B_z$  problem by developing a predictive tool based on machine learning that is trained and tested on 348 ICMEs. By feeding measurements of the ICME into machine learning algorithms, we find that our predictive tool can forecast the  $B_z$  component reasonably well. While our tool does not solve the  $B_z$  problem, it shows promise in forecasting and potentially mitigating the effects of ICMEs on our planet Earth and its inhabitants.

**1 Introduction**

The  $B_z$  component of the interplanetary magnetic field (IMF) largely determines the amount of energy and momentum transferred from the solar wind into the Earth's magnetosphere via magnetic reconnection at the dayside magnetopause (Dungey, 1961). Knowledge of the future  $B_z$  magnitude is integral for monitoring and predicting the energy input into the magnetosphere, ionosphere, and thermosphere. There is a current lack of  $B_z$  forecasting capabilities, which is often referred to as the  $B_z$  problem. In essence, the field of space weather forecasting needs innovation to predict the north-south component ( $B_z$ ) of the IMF in near-Earth space during intense geoeffective events.

Key criteria for intense geoeffective events are extended periods of large southward  $B_z$ , which points opposite to the Earth's magnetic field (Gonzalez & Tsurutani, 1987). The largest southward  $B_z$  disturbances in the IMF are found in coronal mass ejections (CMEs), plasma clouds with embedded magnetic fields that are expelled from the Sun into our solar system (see Webb & Howard, 2012, for a review). At any time, the helio-

sphere is populated with interplanetary coronal mass ejections (ICMEs) that interact with the prevailing ambient solar wind flows and fields. Most of the structure in the ambient solar wind comes from interacting fast and slow solar wind flows (Owens & Forsyth, 2013). Fluctuating magnetic fields in so-called stream interaction regions can also cause weak to moderate geomagnetic activity (Zhang et al., 2007; Kilpua et al., 2017). Although stream interaction regions are a driver of recurrent geomagnetic activity (Tsurutani et al., 2006), the most extreme geomagnetic disturbances are caused by large-scale  $B_z$  perturbations embedded within ICMEs (Echer et al., 2008). It is primarily during ICME events, when accurate  $B_z$  estimates are needed most, that the prediction thereof is most difficult and the  $B_z$  problem is most relevant.

Breakthroughs in the  $B_z$  problem are challenging for many reasons, including observational limitations (see Vourlidas et al., 2019). First, we can not accurately deduce the magnetic properties of CMEs such as magnetic field magnitude, topology, and helicity at the time of formation from observations alone. Radio and EUV off-limb imaging and spectroscopy can inform physics-based models, but we cannot measure these magnetic properties directly. Second, the coronal conditions within the Alfvén surface below approximately 20 solar radii, through which the CME evolves, are unknown. Due to the unknown condition in the corona, we do not understand the origin and early evolution of CMEs well enough to predict their magnetic structure (Vourlidas et al., 2013). Third, we cannot monitor the rotation, compression, deflection, and reconnection of ICMEs in interplanetary space with ambient solar wind fields, which influence the ICME magnetic field structure before they arrive at Earth.

When observations are limited, numerical models can provide insights into the physical conditions. One promising research avenue to tackle the  $B_z$  problem focuses on solving the three-dimensional equation of magnetohydrodynamics (MHD). Examples for MHD codes that incorporate the CME magnetic field structure are SUSANOO-CME (Shiota & Kataoka, 2016), AWMSoM-SWMF (Jin et al., 2017), MAS (Török et al., 2018) and EUHFORIA (Poedts et al., 2020). Although a full physical description is desirable, solving the  $B_z$  problem with MHD codes is challenging, as will be discussed later.

Without a definitive physical solution, we need to study new predictive tools that can enhance our predictive capabilities, and, ideally, inform the boundary conditions of full physics-based models. Today’s predictions of the  $B_z$  component at Earth rely on empirical relationships, statistical extrapolation, pattern recognition, machine learning algorithms, and more. Chen (1996) and Chen et al. (1997) first introduced the idea to use the coherence of magnetic flux ropes in ICMEs to predict their magnetic structure. They found that the  $B_z$  component at Earth can be predicted with lead times of up to 10 hours for well-defined magnetic clouds with a smooth field rotation. Kim et al. (2014) focused on early CME properties and updated their prediction by monitoring the solar wind conditions in space. In contrast, Savani et al. (2015) used remote sensing for predicting the magnetic field components in magnetic clouds at Earth. Here, their prediction relies on the categories introduced in Bothmer and Schwenn (1998) and Mulligan et al. (1998), among other things. More recently, Riley et al. (2017) developed a pattern recognition technique for predicting  $B_z$ , and Owens et al. (2017) used a past analogs method to predict the conditions in the ambient solar wind flow and geomagnetic indices at Earth. Salman et al. (2018) studied historic events to predict the southward interplanetary  $B_z$  periods after interplanetary shocks. Möstl et al. (2018) used solar observations to determine the initial state of the CME, assuming a self-similar expansion. In contrast, dos Santos et al. (2020) developed a deep neural network and an analytical flux rope model to identify the internal structure of ICMEs.

To date, however, scant attention has been paid to using upstream in situ measurements for predicting the  $B_z$  of the magnetic obstacle embedded within ICMEs at the Sun-Earth L1 point. In this study, we present a predictive tool based on machine learning that simplifies the  $B_z$  problem by predicting estimates of the  $B_z$  component for the whole

magnetic flux rope, particularly  $\min(B_z)$  and  $\max(B_t)$ , which can be used as an estimate of the maximum  $B_z$  component. We train, test, and validate the predictive tool on bulk plasma and in situ measurements from 348 ICMEs observed close to a heliocentric distance of 1 AU (Möstl et al., 2017; Möstl et al., 2020).

To simulate an operational space weather forecast, we feed in situ data into the predictive tool as if the ICMEs sweep over the spacecraft in an experimental real-time mode. We then assess how progressively adding data from the ICME sheath and parts of the magnetic obstacle improves the predictive skill. While the predictive tool is far from solving the  $B_z$  problem, it shows reasonable first results in predicting estimates for the lower limit of the  $B_z$  component in ICMEs.

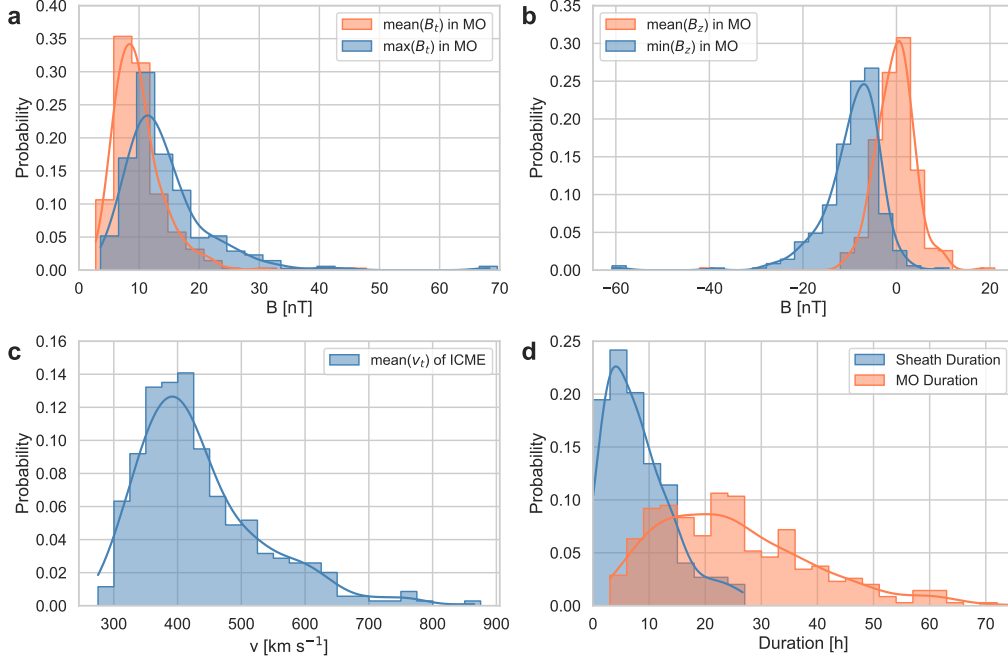
For the sake of consistency and clarity in this study, we follow the definition in Nieves-Chinchilla et al. (2018) and use the term 'magnetic obstacle' to refer to the magnetic structure embedded in an ICME, which can deviate from in situ signatures of an idealized magnetic flux rope in L. Burlaga et al. (1981). We furthermore refer to the sheath as the region of compressed solar wind between the ICME shock front and the leading edge of the magnetic obstacle (Owens et al., 2005) and use the term ICME for the interval of disturbed solar wind conditions including the sheath region and the magnetic obstacle (Rouillard, 2011).

The paper consists of the following parts. After discussion of the data sources in Section 2, Section 3 outlines the machine learning approach, Section 4 outlines the validation analysis, and Section 5 presents the skill of the predictive tool. Section 6 discusses our findings and outlines future perspectives, and Section 7 summarizes the study. Section 8 links to our publicly available online resources and the ICME catalog, in situ solar wind data, and the source code. All the machine learning algorithms are taken from the Python packages Scikit-learn and Keras, which are open-source, straightforward to use, and thoroughly tested.

## 2 Data

At any point in time, the heliosphere is populated by ICMEs, and their physical properties are continually recorded in ICME catalogs. In this study, we use the ICMECAT, an ICME catalog that was originally created during the HELCATS project (Möstl et al., 2017). We have published a major update in Möstl et al. (2020) and now call it the HELIO4CAST ICME catalog or ICMECATv2.0. Here, we use the version last updated on 2021 April 29. It includes 558 ICMEs observed close to 1 AU, at the Sun-Earth L1 point and by STEREO-A/B, during the time interval 2007 January 1 to 2021 April 1. ICME events are added manually to this living catalog, guided by the criteria in Nieves-Chinchilla et al. (2018). It contains only events that show clear signatures of magnetic structure, called magnetic obstacles. A large number of events, frequent updates, and open access (see Section 8) are the main advantages and the reasons for this choice.

To train, validate, and test machine learning algorithms for predicting  $B_z$ , we use bulk plasma and in situ measurements for ICMEs in ICMECATv2.0 that are close to a heliocentric distance of 1 AU. In particular, we study in situ measurements from the MFI and SWE instruments on the Wind spacecraft (Ogilvie et al., 1995; Lepping et al., 1995) and the IMPACT and PLASTIC instruments on the STEREO-A and STEREO-B spacecraft (Luhmann et al., 2008; Galvin et al., 2008). From the 558 ICMEs in ICMECATv2.0 observed by WIND, STEREO-A, and STEREO-B, we focus on 362 ICMEs (or 65%) that show either sheath region signatures or a density pileup in front of a magnetic obstacle. This selection results in 149 ICMEs in Wind, 135 ICMEs in STEREO-A, and 78 ICMEs in STEREO-B. After cleaning the data and removing events with too many missing data points in the measurements, we end up with 348 ICMEs, with 149 ICMEs in Wind, 123 ICMEs in STEREO-A, and 76 ICMEs in STEREO-B.



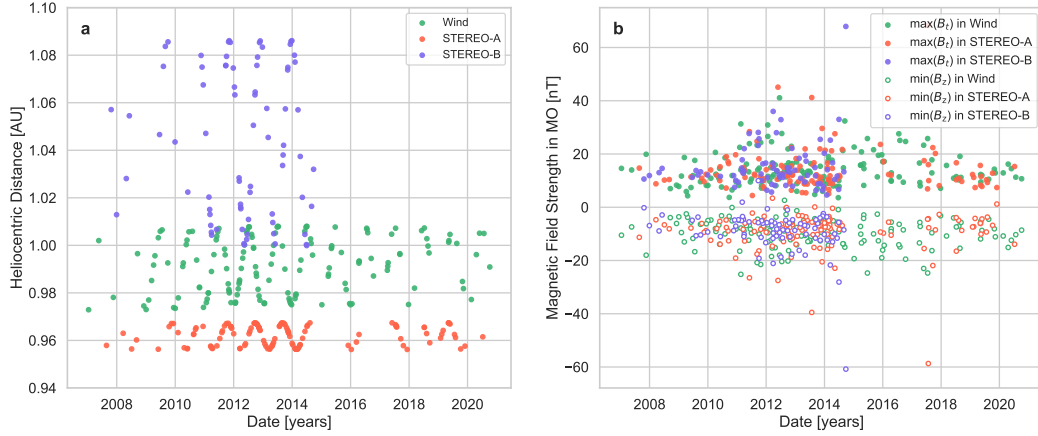
**Figure 1.** The probability distribution functions of the physical properties of 348 ICMEs under scrutiny. (a) The mean and maximum total magnetic field in the magnetic obstacle; (b) the minimum and mean  $B_z$  in the magnetic obstacle; (c) the mean bulk plasma speed in the ICME including the sheath and magnetic obstacle; and (d) the sheath and magnetic obstacle durations.

Figure 1 shows the probability distribution functions of physical properties of the 348 ICMEs. These physical properties include the mean and maximum of the total magnetic field ( $B_t$ ) in the magnetic obstacle, mean and minimum of  $B_z$  in the magnetic obstacle, mean of the bulk plasma speed ( $v_t$ ) in the ICME, and the duration of the sheath and magnetic obstacle. The value range of ICME and magnetic obstacle properties that we use for machine learning is as follows. The average duration of the sheath region is  $9.0 \pm 6.0$  h, and that of the magnetic obstacle is  $25.2 \pm 14.6$  h. The sheath region is defined as the interval between the *icme.start.time* and the *mo.start.time* parameters in the ICME catalog, and the magnetic obstacle ranges from *mo.start.time* to *mo.end.time*. The mean maximum value of  $B_t$  in the magnetic obstacle is  $14.3 \pm 7.6$  nT, and the mean minimum value of  $B_z$  in the magnetic obstacle is  $-9.4 \pm 6.8$  nT.

Figure 2a shows the heliocentric distance as a function of time for the 348 ICMEs, with the color indicating the observing spacecraft. Figure 2b illustrates the maximum values of the total magnetic field  $B_t$  and the minimum of the  $B_z$  component in the magnetic obstacles. These two properties are the targets we want to predict. To do so, we train machine learning algorithms with ICME properties including  $B_t$ ,  $v_t$ , the magnetic field components ( $B_x$ ,  $B_y$ ,  $B_z$ ), and the proton temperature ( $T_p$ ) and density ( $N_p$ ).

### 3 Machine Learning

To predict the  $B_z$  component in the magnetic obstacle embedded within an ICME, we train machine learning algorithms on the properties of 348 ICMEs. Figure 3 illustrates the main idea. Feature values computed in the ICME sheath region and parts of the magnetic flux rope (window delineated by green vertical lines) are used as input to machine



**Figure 2.** Properties of the 348 ICMEs in the catalog. (a) Heliocentric distance for each ICME event as a function of time, observed with Wind (green), STEREO-A (red), and STEREO-B (blue); (b) Maximum total magnetic field (filled circles)  $B_t$  and minimum value of the  $B_z$  component (open circles) in the magnetic obstacle (MO) of the ICME for each event as a function of time.

learning to predict the minimum of the  $B_z$  component in the magnetic obstacle (red horizontal line). The three events in Figure 3(a–c) represent ideal, average, and poor  $B_z$  predictions of the final tool, where the red horizontal lines show the prediction and the blue horizontal lines show the observation. The ideal, poor, and average examples correspond to an absolute error close to zero, the median absolute error, and the 75% percentile in the validation.

In the following, we introduce the predictive tool. To do so, we specify the features and targets, study different machine learning algorithms, split the ICME catalog into training and testing sets, perform hyperparameter tuning to optimize the machine learning algorithms, and test the  $B_z$  prediction in an experimental real-time mode.

### 3.1 Features and Targets

We compute the features for machine learning from in situ plasma and magnetic field measurements of 348 ICMEs. In particular, we examine the timelines of 7 different physical properties ( $B_t$ ,  $B_x$ ,  $B_y$ ,  $B_z$ ,  $v_t$ ,  $T_p$ ,  $N_p$ ) and compute 6 statistical measures for each of them. The measures that serve as features for machine learning include the mean value, standard deviation, minimum and maximum values, the ratio between the maximum and minimum values, and the ratio between the mean value and standard deviation, also known as the coefficient of variation. These features are calculated for either the sheath region alone or the sheath region plus several hours of the magnetic obstacle interval (for example, using the first 4 hours into the magnetic obstacle, as illustrated before). We moreover studied combinations of the physical properties, including  $v_t B_z$ ,  $v_t B_t$ ,  $v_t^2$ ,  $B_t^2$ , but did not see any significant improvement in the validation metrics.

By computing feature values for all selected ICME events, we create a  $42 \times 348$  feature matrix with 14616 entries that serves as input to the machine learning algorithms. We define two targets that we want to predict inside the magnetic obstacle: (1) the minimum of the  $B_z$  component,  $\min(B_z)$ ; and (2) the maximum of the total magnetic field,  $\max(B_t)$ .

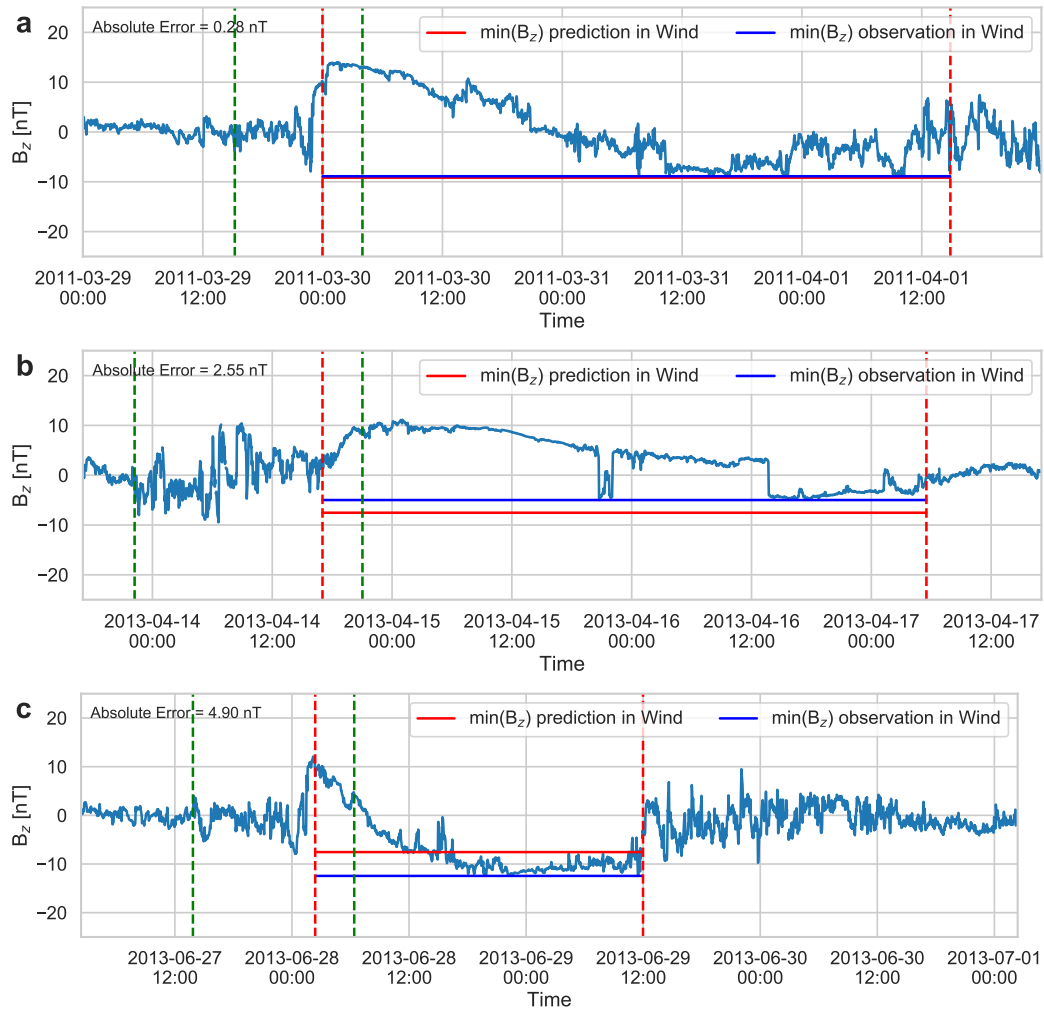


**Figure 3.** Comparison of the predicted minimum value of the  $B_z$  component in the magnetic obstacle using a Gradient Boosting Regressor (red) with the observation (blue). The absolute errors are close to the ideal prediction (a), median validation error (b), and the 75% percentile in the absolute error (c), respectively. The vertical green dashed lines mark the time interval where we compute the feature values, and the vertical red dashed lines mark the magnetic obstacle where we predict  $B_z$ . In these three examples, we use the ICME sheath and the first 4 hours of the magnetic obstacle indicated by the green dashed lines as input for the  $\min(B_z)$  prediction indicated by the horizontal red line.

### 3.2 Machine Learning Algorithms

We use a linear regressor (LR), random forest regressor (RFR), and gradient boosting regressor (GBR, see Friedman, 2001) from the widely-applied Python package Scikit-Learn to train a model. We select the RFR and the GBR from many learners because they provide the most accurate predictions for the problem at hand, are robust algorithms for training, and are efficient to implement and tune. The RFR and GBR both rely on decision trees, which show powerful predictive skill when combined in an ensemble of hundreds of trees, usually referred to as a forest. We also provide the results from a simple LR that acts as a benchmark against which future versions of the predictive tool and studies can be easily compared.

### 3.3 Training and Testing

For every ICME, we have computed 6 statistical measures for 7 physical properties, resulting in a total of 42 features. We identify those features that affect the prediction the most. To validate the real-world performance, we split the input data into training and testing data. This final hold-out testing set is not used in training. By using the testing set for assessing the prediction, we attempt to extrapolate the model’s skill to unseen behavior. The training set includes 243 ICMEs, and the testing set includes 105 ICMEs, randomly selected. This selection corresponds to 70% and 30% of all events. During training, we apply stratified 5-fold cross validation, in which a randomly selected subset (1/5th) of the training data set is kept aside while the model is trained on the remaining 4/5ths. Each ‘fold’ of the data is cycled through to produce five trained models. Out of the five trained models, the one that performs best on the unseen data from the reserved subset is kept as the final model. We also apply early stopping, where model training is stopped some steps before it reaches the minimum in the loss function to prevent over-fitting to the data.

### 3.4 Hyperparameter Tuning

We perform hyperparameter tuning for the RFR and GBR for the selected set of features. To do so, we use a grid search and test combinations of parameter sets. The parameters for the two models include the learning rate, the maximum depth of each tree, minimum number of samples to define a node split, minimum number of samples per leaf, and the number of trees/estimators, resulting in 4 parameters for GBR tuning and 5 parameters for RFR tuning. We examine every point in this 4D (5D) parameter space within specified parameter ranges and use each set of parameters to train the GBR (RFR). The parameter set with the best scoring measure is used for training. After the grid search, we create a model including 200 decision trees (300), where the maximum depth of each tree is 3 (5) for the GBR (RFR). The minimum number of samples to define a node split or set a leaf was also defined in hyperparameter tuning for the RFR and GBR.

### 3.5 Experimental Real-Time Mode

We furthermore attempt to simulate an operational space weather forecast. To do so, we feed the features from the magnetic sheath and magnetic obstacle (Section 3.1) into three machine learning algorithms (Section 3.2) to predict  $\max(B_t)$  and  $\min(B_z)$  as if an ICME sweeps over the spacecraft in an experimental real-time mode. We start with the features computed from the magnetic sheath and progressively add in situ measurements from the magnetic obstacle in a 1 hour cadence. This approach results in a string of separately trained algorithms applied in succession for each input time window. Conducting such an analysis is useful because it allows us to estimate the reliability of the predictive tool in an operational situation, and furthermore points to possible weaknesses in the methodology.

**Table 1.** Overview of point-to-point comparison metrics.

Metric	Short Name	Definition
Mean error	ME	$\frac{1}{n} \sum_{k=1}^n (f_k - o_k)$
Mean square error	MSE	$\frac{1}{n} \sum_{k=1}^n (f_k - o_k)^2$
Mean absolute error	MAE	$\frac{1}{n} \sum_{k=1}^n  f_k - o_k $
Root mean square error	RMSE	$\sqrt{\frac{1}{n} \sum_{k=1}^n (f_k - o_k)^2}$
Skill score	SS	$1 - \frac{\text{MSE}_{\text{pred}}}{\text{MSE}_{\text{ref}}}$

In this way, we study how progressively adding in situ measurements from the magnetic obstacle improves the  $B_z$  prediction. We assess how many hours from the magnetic sheath and magnetic obstacle are required to achieve a certain accuracy in magnetic obstacle  $\max(B_t)$  and  $\min(B_z)$  predictions.

## 4 Validation Analysis and Metrics

We assess the skill of the machine learning algorithms for predicting  $\min(B_z)$  and  $\max(B_t)$  with widely-applied validation metrics. These metrics are computed from a comparison between measurements and predictions in terms of continuous and binary variables. Contrary to continuous variables that can take on any real numbers, binary variables are categorical such as event and non-event predictions (see, for instance, Owens et al., 2005; Reiss et al., 2016; Wold et al., 2018). Focusing on both approaches, we compute average errors from the comparison of the predicted and observed magnetic fields, and then investigate an event-based validation analysis.

### 4.1 Point-to-point Metrics

First, we compare the predictions with observations in terms of statistical measures such as the mean, median, and standard deviation. These basic measures contain important information on the underlying statistical distribution of the predicted and observed values indicating, for example, if a model tends to over- or under-estimate the measurement.

In addition, we study the model accuracy in terms of error functions such as the mean error (ME), mean absolute error (MAE), and the root mean square error (RMSE). Table 1 summarizes these error functions, where  $(f_k, o_k)$  is the  $k$ -th element of  $n$  pairs of forecasts and observations. Although strictly speaking not an error function, we also include the Pearson correlation coefficient (PCC) in the analysis.

Next, we examine if our predictive tool is more useful than a simple baseline model. Baseline models are a valuable diagnostic to determine the skill of a novel model approach relative to a naive prediction. Baseline models in the space weather community often rely on the mean value of past observations (see, for example, Owens, 2018). For the sake of consistency, we define our baseline model as the mean value of all the targets we train our machine learning algorithms on.

In this context, the skill score (SS) is a measure that quantifies the skill of a forecast in comparison to the baseline model. Table 1 shows the definition of SS, where  $\text{MSE}_{\text{pred}}$

**Table 2.** Overview of binary metrics defined by the entries of a contingency table.

Metric	Short Name	Definition
True Positive Rate	TPR	$\frac{TP}{TP+FN}$
False Positive Rate	FPR	$\frac{FP}{FP+TN}$
Threat Score	TS	$\frac{TP}{TP+FP+FN}$
True Skill Statistics	TSS	$TPR - FPR$
Bias	BS	$\frac{TP+FP}{TP+FN}$

is the mean square error of the prediction, and  $MSE_{ref}$  is the MSE of the reference baseline model. A negative SS means the model is worse than the baseline model, a SS of 0 means the model is equal to the baseline model, whereas 1 indicates an ideal prediction.

## 4.2 Binary Metrics

By categorizing each  $\min(B_z)$  and  $\max(B_t)$  prediction in terms of event/non-event predictions, we complement the analysis in the previous section. The advantages are plentiful as outlined in Owens (2018). First, error functions give equal importance to weak and strong magnetic field strength. Some users of our predictive tool, however, are only interested in the ability of forecasting events above a certain threshold, while smaller events are less important. Second, outliers in the prediction significantly affect point-to-point comparison metrics. For users wanting to react when the event exceeds a defined threshold, an alternative is to consider each prediction as an event/non-event prediction.

To define events and non-events in the observation and prediction, we use a threshold value equal to the mean value of all 105 ICMEs in the test data. Through the cross-check of event and non-event combinations in the observed and predicted MFR properties, we count the number of hits (true positives; TPs), false alarms (false positives; FPs), misses (false negatives; FNs), and correct rejections (true negatives; TNs). Summarized in the so-called contingency table, a TP is a correctly predicted event, while an FN is an event that was not predicted. On the other hand, an FP is a predicted event that was not observed, and a TN is a correctly predicted non-event.

Table 2 shows skill measures that we compute from the entries of the contingency table. Here the ratio between the number of predictions and observations, also known as Bias (BS), shows the tendency of the machine learning algorithms to over- or underestimate the number of events. In addition, the true skill statistics (TSS) lies in the range  $[-1, 1]$ , where an ideal prediction would have the value 1 (or -1 for an optimum inverse prediction), and a TSS of 0 means no skill. One benefit of the TSS is that it uses all the elements in the contingency table and that it is unbiased by the proportion of predicted and observed events (see Hanssen & Kuipers, 1965; Bloomfield et al., 2012).

## 5 Results

We validate the predictive tool on data unused in our machine learning investigation, which is the test data set with 105 ICMEs. To provide a fair assessment throughout the solar cycle, the 105 ICMEs are randomly selected from 2007 January 1 to 2021

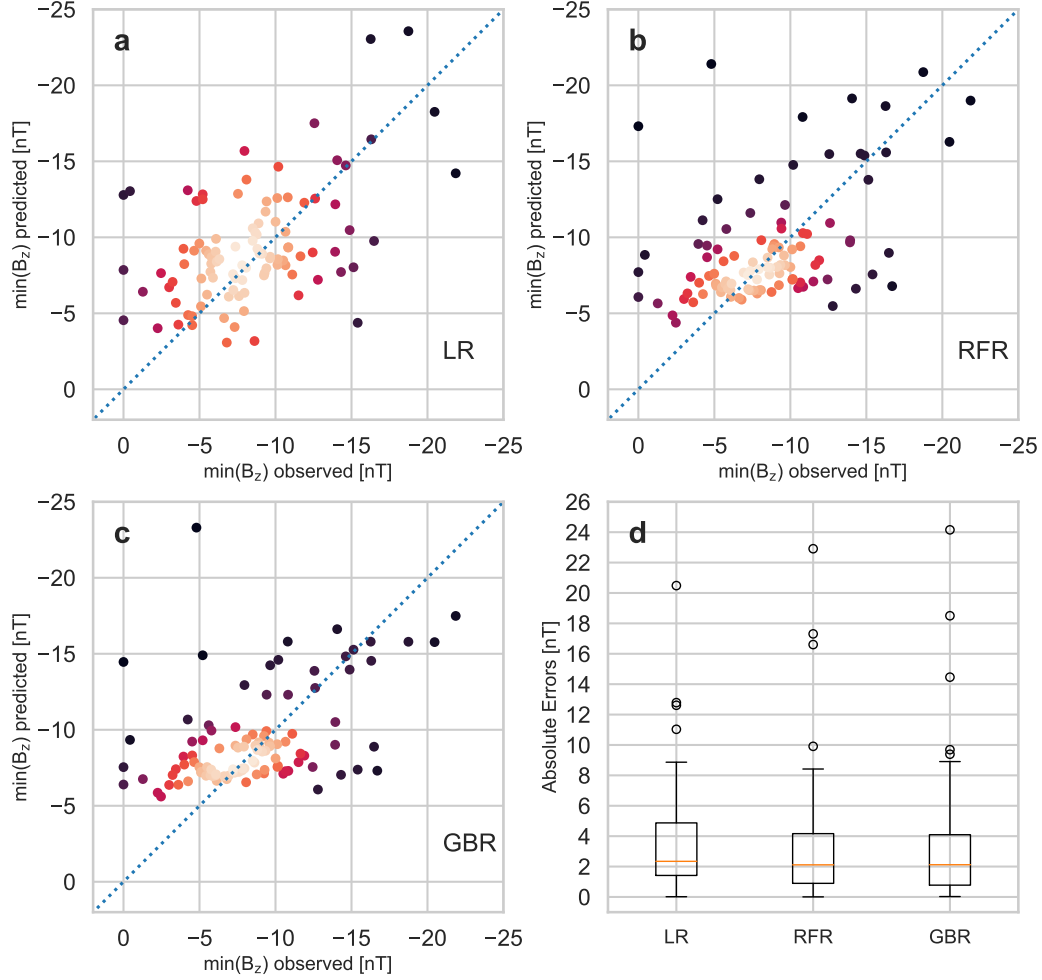


**Figure 4.** Comparison of the predicted and observed minimum value of the  $B_z$  component with three different machine learning algorithms, where the color scales with the density of the data points. (a) Linear Regressor; (b) Random Forest Regressor; (c) Gradient Boosting Regressor; (d) absolute error of the different algorithms applied to the ICMEs in the test data set. Data from the sheath region and the first 4 hours of the magnetic obstacle were used to train these models.

April 1. We then let each ICMEs sweep over the spacecraft in an experimental real-time mode and assess how additional information from several hours inside the magnetic flux rope improves the predictive skill.

To illustrate the skill of the predictive tool, we plot the prediction of the minimum value of the  $B_z$  component versus the observation. For this illustration, we feed data from the sheath region and 4 hours from the beginning of the magnetic obstacle into the three trained machine learning algorithms. Figure 4(a–c) shows a comparison of the prediction and observation of  $\min(B_z)$  for the linear regressor (LR), random forest regressor (RFR), and the gradient boosting regressor (GBR), respectively. Figure 4(d) shows the boxplot for the absolute error of the different algorithms. Here the red line is the median error (50<sup>th</sup> percentile), the edges are the 25<sup>th</sup> and 75<sup>th</sup> percentiles, the whiskers show the  $\pm 2.5\sigma$  range covering 99.3% of the data, and the outliers are plotted as black circles. Agreement of the data points with the blue dashed lines in Figure 4(a–c) indicate

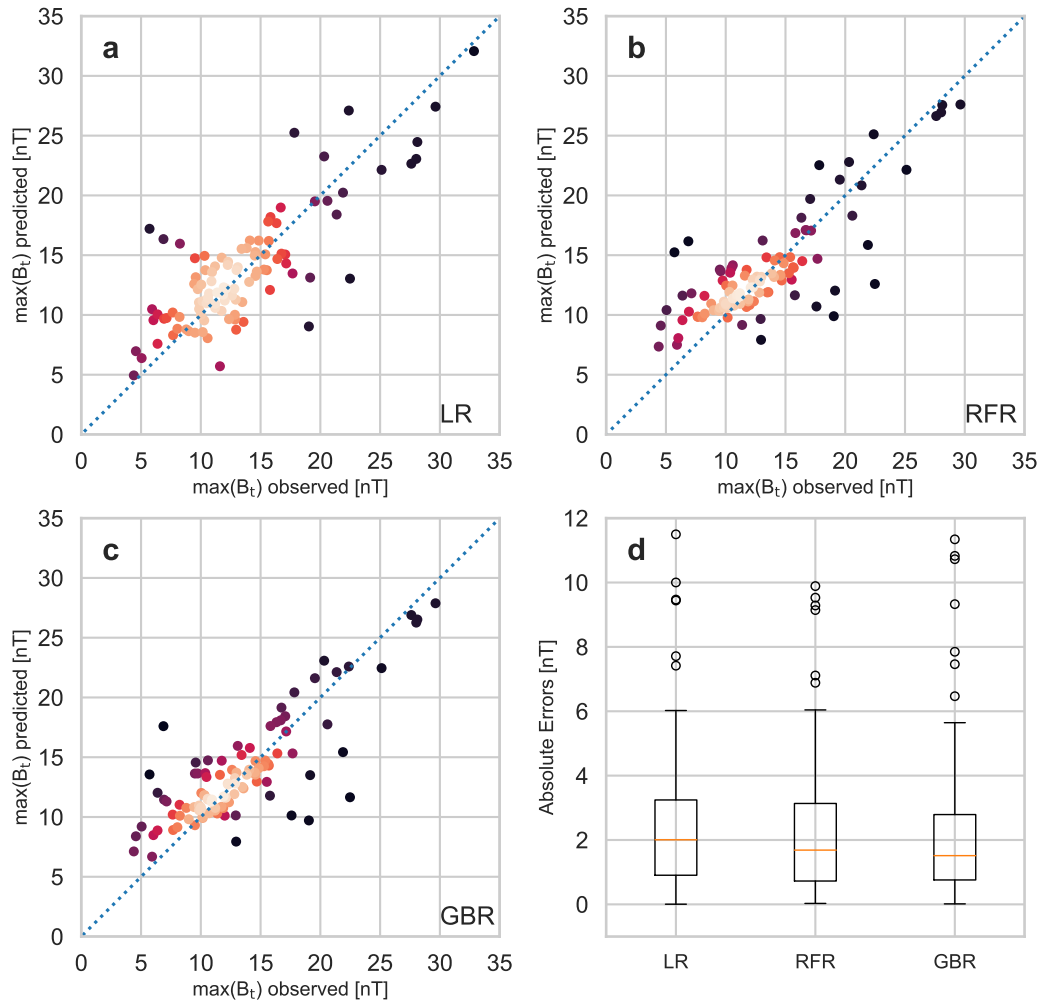


**Figure 5.** Comparison of the predicted and observed maximum value of the total magnetic field with three different machine learning algorithms, where the color scales with the density of the data points. (a) Linear Regressor; (b) Random Forest Regressor; (c) Gradient Boosting Regressor; (d) absolute error of the different algorithms applied to the ICMEs in the test data set. Data from the sheath region and the first 4 hours of the magnetic obstacle were used to train these models.

**Table 3.** Predictive abilities in terms of arithmetic mean (AM), standard deviation (SD), mean error (ME), mean absolute error (MAE), root mean square error (RMSE), the skill score (SS) relative to the simple mean value of all events, and the Pearson correlation coefficient (PCC). We use the sheath plus the first 4 hours of the MO to predict  $\min(B_z)$  and  $\max(B_t)$ , respectively.

Target	Model	AM [nT]	SD [nT]	ME [nT]	MAE [nT]	RMSE [nT]	SS	PCC
$\min(B_z)$	LR	-9.67	12.26	0.61	4.80	11.97	-2.24	0.32
$\min(B_z)$	RFR	-9.47	4.58	0.41	3.16	4.73	0.49	0.70
$\min(B_z)$	GBR	-9.58	4.12	0.52	3.12	4.77	0.49	0.71
$\min(B_z)$	Observation	-9.06	6.65	-	-	-	-	-
$\max(B_t)$	LR	14.18	11.15	-0.28	3.64	9.48	-0.55	0.54
$\max(B_t)$	RFR	14.09	5.68	-0.19	2.41	3.79	0.75	0.88
$\max(B_t)$	GBR	14.18	6.33	-0.29	2.23	3.20	0.82	0.91
$\max(B_t)$	Observation	13.89	7.63	-	-	-	-	-

the best performance. In comparison, the PCC for the LR, RFR, and GBR is 0.32, 0.70, and 0.71, respectively. In addition to the PCCs, we compute the p-values to test the null hypothesis that the relation between prediction and measurement is statistically insignificant. While a low p-value ( $< 0.05$ ) indicates that we can reject this null hypothesis, a larger p-value confirms it. We find that all the predictions are statistically significant because the p-value for the LR is equal to 0.001, and the p-values for the RFR and GBR are equal to 0. Although the LR results do not look promising, more reasonable results are achieved by the RFR and GBR.

Figure 5 shows the same illustration for the maximum value of the total magnetic field  $\max(B_t)$ . All three algorithms show considerably higher accuracy in comparison to the previous results for  $\min(B_z)$ . In particular, the PCC for the LR, RFR, and GBR is 0.54, 0.88, and 0.91, respectively. Again, we find that the relation between observation and prediction is statistically significant for all the algorithms because the p-values are equal to 0. Both the RFR and GBR show promise for predicting  $\max(B_t)$  as an estimate of the  $B_z$  component.

For the 105 ICMEs under scrutiny in this section, we found that the predictive skill of the machine learning algorithms stays nearly constant throughout the solar cycle, and there are no significant differences among the three spacecraft.

For a more detailed error analysis, we compute point-to-point metrics as defined in Table 1. The first three rows in Table 3 show the results of the different algorithms for  $\min(B_z)$ , and the columns show the corresponding values. The fourth row in the table shows the arithmetic mean (AM) and the standard deviation (SD) of the observation. From the results for  $\min(B_z)$ , we see that the RFR and GBR outperform the LR in all metrics. While the MAE for the RFR and GBR is 3.16 nT and 3.12 nT, the MAE for the LR is 4.80 nT. Also, the PCC for the RFR and GBR is 0.70 and 0.71, the PCC for the LR is 0.32. This trend is confirmed in the SS comparing the skill to a baseline model. We find that the LR is worse than the baseline model with negative SS, and the results for the RFR and GBR are 0.49, where 0 would indicate the same skill as the baseline, and 1 would indicate an optimum forecast.

The last four rows in Table 3 show the results of the different machine learning models for predicting  $\max(B_t)$ . Again we find that the RFR and GBR outperform the LR. For example, the MAE for the RFR and GBR is 2.41 nT and 2.23 nT, the MAE for the

LR is 3.64 nT. Focusing on the differences between the RFR and GBR for both targets, we find that both perform similarly, with the GBR providing slightly better results.

We furthermore investigate an operational setting where an ICME sweeps over the spacecraft. In this experimental real-time mode, we quantify how additional information from the magnetic flux rope improves the skill of the machine learning algorithms. Figure 6 shows the skill of a string of trained RFR and GBR models for the prediction of  $\min(B_z)$  and  $\max(B_t)$ . The first data point at 0 hours denotes the start of the magnetic obstacle where features are computed only from the sheath region. With increasing time elapsed from the magnetic obstacle start, more information from the target is included in the input data. As expected, we find that including more information from the magnetic obstacle improves the accuracy of the predictive skill. As an example, the PCC for the  $\min(B_z)$  RFR prediction and  $\max(B_t)$  RFR prediction improves in the first 4 hours by approximately 14% and 13%. We also find that more data from the magnetic obstacle improves the LR predictions (not shown in the plot). However, the variations in the LR predictions are significantly larger in comparison to the RFR and GBR when seeing more from the magnetic obstacle.

We complement this analysis with an event-based validation study. We specifically use the mean value of the test data with 105 ICMEs as an event threshold. Values below a threshold of  $-9.06$  nT for  $\min(B_z)$  and above  $13.89$  nT for  $\max(B_t)$  signify an event, and all other values are not events. As discussed in Section 3.2, the results of this analysis can be summarized in a contingency table, from which we can compute the measures defined in Table 2. Table 4 lists the resulting measures for the different learners. In terms of an actionable prediction, the RFR provides the best results with a TSS of 0.30, followed by the GBR with a TSS of 0.28, and the LR with a TSS of 0.18. Again we find a clear gap between the LR and the other two models. These differences indicate that the results by the LR are not only less promising in predicting the exact values but also in predicting the severity of the ICME.

In quantitative measures, we find that the GBR was able to predict if  $\min(B_z)$  is below  $-9.06$  nT in 77% of all observed ICMEs in this category. On the other hand, 47% of all the events above  $-9.06$  nT were erroneously classified as being below this threshold by the GBR. When focusing on  $\max(B_t)$  as an approximation, the results are significantly better. More specifically, the GBR was able to predict if  $\max(B_t)$  is above  $13.89$  nT in 77% of all observed ICMEs in this category, and only 11% of all the events below  $13.89$  nT were erroneously classified.

For end-users interested only in the most extreme events, we have conducted an additional analysis where we focus only on the 15 most decisive events in terms of  $\min(B_z)$  and  $\max(B_t)$ . For the 15 strongest observed events in terms of  $\min(B_z)$  below a TH of  $-13.93$  nT, we find that the LR, RFR, and GBR can correctly predict 8, 9, and 10 events below this event threshold, respectively. Focusing on the 15 strongest events in  $\max(B_t)$  above a TH of  $19.05$  nT, we find that the LR, RFR, and GBR can correctly predict 12, 11, and 11 events, respectively.

In summary, we find that the RFR and GBR provide promising first results and justify their use. While not solving the  $B_z$  problem, this prototype predictive tool can narrow down the extent of the  $B_z$  component expected during the ICME arrival at Earth. We find that the predictive ability of the tool increases considerably with additional information as an ICME sweeps over the spacecraft.

## 6 Discussion

A traditional way of approaching the  $B_z$  problem is to simulate the propagation of ICMEs with MHD codes. Examples are SUSANOO-CME (Shiota & Kataoka, 2016), AWSoM-SWMF (Jin et al., 2017), MAS (Török et al., 2018), and EUHFORIA (Poedts

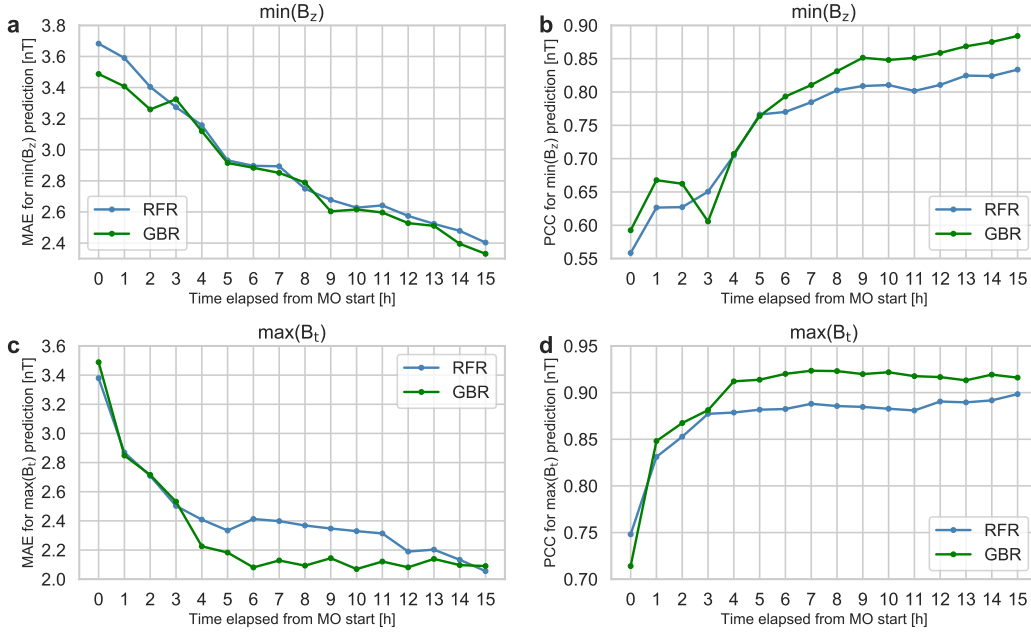


**Figure 6.** Effect of the time elapsed from the magnetic obstacle start on the predictive ability of the different machine learning models. (a) MAE for the  $\min(B_z)$  prediction; (b) PCC for the  $\min(B_z)$  prediction; (c) MAE for the  $\max(B_t)$  prediction; (d) PCC for the  $\max(B_t)$  prediction.

**Table 4.** Contingency table and skill measures for an event-based validation analysis. The table shows the number of observed ( $N_{\text{obs}}$ ) and predicted ( $N_{\text{pred}}$ ) events, hits (true positives; TPs), false alarms (false positives; FPs), misses (false negatives, FNs), correct rejections (true negatives, TNs), and the metrics derived from these entries including: the true positive rate (TPR) and false positive rate (FPR), threat score (TS), true skill statistics (TSS), and bias (BS).

Target	Model	$N_{\text{obs}}$	$N_{\text{pred}}$	TP	FP	FN	TN	TPR	FPR	TS	TSS	BS
$\min(B_z)$	LR	60	60	39	21	21	24	0.65	0.47	0.48	0.18	1.00
$\min(B_z)$	RFR	60	67	46	21	14	24	0.77	0.47	0.57	0.30	1.12
$\min(B_z)$	GBR	60	68	46	22	14	23	0.77	0.49	0.56	0.28	1.13
$\max(B_t)$	LR	39	41	28	13	11	53	0.72	0.20	0.54	0.52	1.05
$\max(B_t)$	RFR	39	34	28	6	11	60	0.72	0.09	0.62	0.63	0.87
$\max(B_t)$	GBR	39	37	30	7	9	59	0.77	0.11	0.65	0.66	0.95

et al., 2020). These MHD codes include the magnetic flux rope structure and simulate the ICME evolution from near the Sun into interplanetary space. Although a full physics-based description is desirable, a breakthrough in solving the  $B_z$  problem with MHD codes alone is challenging. On the one hand, the boundary conditions for all MHD codes are based on solar magnetic field measurements, but these are known to have large inherent uncertainties. Additionally, small uncertainties in the initial conditions of a CME grow to large errors in the predicted magnetic field components at 1 AU, demonstrated e.g. with semi-empirical forward models by Kay and Gopalswamy (2018) and Möstl et al. (2018). Even with flux-transport models based on Sun-Earth line observations, it is difficult to develop a time-dependent coronal magnetic model, which is needed to capture the early CME evolution. On the other hand, the solar corona is not strictly an MHD

environment. While an MHD simulation can describe the large-scale coronal conditions within the Alfvén surface, the evolution of CMEs occurs over a broad range of spatial scales. Small-scale processes such as triggering instabilities are essential to capture the whole picture. Without a definitive physical solution, we need to study new predictive tools that can enhance  $B_z$  prediction capabilities, and ideally, provide constraints for physics-based models.

In this context, we have studied the hypothesis that upstream in situ measurements of the sheath region and the first few hours of the magnetic flux rope of the ICME are useful to predict estimates of the  $B_z$  component. To test this hypothesis, we developed a predictive tool based on machine learning that is trained and tested on 348 ICMEs. We found that the tool can predict the minimum value of the  $B_z$  component (PCC= 0.71) and the maximum value of the total magnetic field  $B_t$  (PCC= 0.91) in the magnetic obstacle in reasonable agreement with observations. While the investigated hypothesis certainly does not solve the  $B_z$  problem, it shows promising first results for ICMEs that have a magnetic flux rope signature, and its application might be useful for operational space weather forecasting. For an application in an operational context, we computed the best-case warning time when we assume immediate data access and model application to a real ICME. To do so, we compute the lead time between the arrival of the magnetic obstacle and the peak in the  $\min(B_z)$  and  $\max(B_t)$  values. For  $\min(B_z)$ , we find that the average warning time is 9.68 h, the median warning time is 5.87 h, and the maximum warning time is 46.15 h. The same analysis for  $\max(B_t)$  showed that the average warning time is 5.98 h, the median warning time is 2.53 h, and the maximum warning time is 33.55 h.

To put our results into context, we want to discuss the following three limitations of our study. First, we have significantly reduced the complexity of the  $B_z$  problem by focusing on estimates of the  $B_z$  component for the whole magnetic flux rope, specifically  $\min(B_z)$  and  $\max(B_t)$ . Focusing on these large-scale statistics of the magnetic flux rope is considerably easier than predicting the temporal evolution of  $B_z$ . Nevertheless, the ability of our prototype to predict  $\min(B_z)$ , a proxy for ICME geoeffectiveness, is essential in an actionable forecast.

Second, we have trained and tested the machine learning algorithms on ICMEs that occurred between the years 2007 to 2021 using the ICMECATv2.0 catalog. The main criterion was that the ICMEs needed to show either sheath region signatures or a density pileup in front of a magnetic obstacle. This criterion reduced the number of ICMEs to approximately 65% of the original catalog. The expected magnetic flux rope signatures in this study include increasing magnetic field strength, rotation of at least one field component, and plasma- $\beta < 1$  (L. F. Burlaga, 1988). These signatures are not always observed by satellites (Rouillard et al., 2009; Wood & Howard, 2009; Vourlidas, 2014). We know that flux ropes undergo deformation and distortion during their dynamic evolution, often leading to significant deviation from an idealized flux rope structure (Riley et al., 2006; Savani et al., 2010; Nieves-Chinchilla et al., 2012). Therefore, an open question is how well we can extrapolate the predictive skill presented here to an operational space weather forecast.

Third and in the context of the last point, we know that the success of the predictive tool in any operational setting will depend on accurate automated ICME detection in mission data as introduced in Telloni et al. (2019); Nguyen et al. (2019). Combining our predictive tool with an automated ICME detection algorithm introduces new challenges. For example, we would need to understand the effect of a timing error in the automated ICME detection on the coupled predictive tool for the  $B_z$  prediction. More research is required to assess these uncertainties and understand their effect on the robustness and reliability of the  $B_z$  prediction.

In the future, we will work on several topics to improve upon this prototype. Besides coupling our predictive tool with an automated ICME detection algorithm, we will

also work on new strategies to forecast the temporal evolution of the  $B_z$  component. Here, our approach is two-fold. Initially, a data driven machine learning approach to predict the temporal evolution of the  $B_z$  component is envisaged. Next, we will explore the integration of a semi-empirical magnetic flux rope model as discussed in Weiss, Möstl, Amerstorfer, et al. (2021) and Weiss, Möstl, Davies, et al. (2021) in our framework. The advantage of this technique is that it can model the CME flux ropes in conjunction with an approximate Bayesian computation (ABC) algorithm that fits the model to in situ magnetic field measurements. We will study if the CME flux rope model can fit the rest of the magnetic flux rope from the first few hours of the ICME. For both approaches, we aim to deduce error boundaries for the  $B_z$  prediction.

In a long-term vision, our predictive tool could make use of mission data from a space weather monitor closer to the Sun using solar sail technology (West, 2004). When the space weather monitor is placed near the Sun-Earth line at approximately  $3 \times 10^6$  km upstream from Earth or twice the distance to L1, the warning time compared to L1 satellites is doubled. In other words, for an ICME traveling with 400 km/s (which is close to the median speed of the ICMEs under scrutiny), the lead time before the event arrives at Earth increases from approximately 1 hour to 2 hours. Since the present methodology is developed and tested for three different spacecraft, our predictive tool could be expanded to future space missions orbiting at 1 AU when differences among instrumentation are taken into consideration.

To allow the community to compare future studies with our findings, the source code, ICMECATv2.0 catalog, and related data are available online as outlined in Section 8.

## 7 Summary

The capacity of ICMEs to cause extreme geomagnetic storms fundamentally depends on their internal plasma structure and their  $B_z$  magnetic field. At present, we can not predict the  $B_z$  magnetic field component with sufficient warning time before the ICME arrival at Earth. This conundrum is often called the  $B_z$  problem.

We shine new light on the  $B_z$  problem by studying the research question if upstream in situ measurements of the ICME sheath region and the first few hours of the magnetic flux rope are sufficient for predicting the  $B_z$  component. To do so, we developed a predictive tool based on machine learning that is trained and tested on 348 ICME events observed by the Wind, STEREO-A, and STEREO-B spacecraft. We train machine learning models to output the minimum value of the  $B_z$  component and the maximum value of the total magnetic field  $B_t$  in the magnetic obstacle.

To test our predictive tool in an experimental real-time mode, we let the ICMEs sweep over the spacecraft and assess how continually feeding new information into the tool improves the  $B_z$  predictions.

Our study shows that the predictive tool can predict the minimum value of the  $B_z$  component (MAE= 3.12 nT, PCC= 0.71) and the maximum value of the total magnetic field  $B_t$  (MAE= 2.23 nT, PCC= 0.91) in the magnetic obstacle in reasonable agreement with observations. While the investigated hypothesis does not solve the  $B_z$  problem, the first version of the predictive tool shows reasonable results for ICMEs that have a clear magnetic flux rope signature, and its application might be suited for operational space weather forecasting in the future.

## 8 Data Availability Statement

The solar wind in situ data are available as python numpy arrays at <https://doi.org/10.6084/m9.figshare.12058065.v8> (updated on 2021 April 29) and were originally down-

loaded from <https://stereo-ssc.nascom.nasa.gov> (STEREO) and <https://spdf.gsfc.nasa.gov/pub/data/wind/> (Wind). The current version of the ICME catalog ICME-CATv2.0, version 6 updated on 2021 April 29 and as published on the data sharing platform figshare, was used in this study: <https://doi.org/10.6084/m9.figshare.6356420.v6>. (The most up-to-date version can be found at <https://heliocast.space/icmecat>.) The paper source code is available at [https://github.com/heliocast/Papers/tree/master/Reiss2021\\_MLrope](https://github.com/heliocast/Papers/tree/master/Reiss2021_MLrope).

## Acknowledgments

M.A.R., C.M., R.L.B., U.V.A., T.A., A.J.W., and J.H. thank the Austrian Science Fund (FWF): P31659-N27, P31521-N27, and P31265-N27. Europlanet 2024 RI has received funding from the European Union's Horizon 2020 research and innovation programme under grant agreement No 871149.

## References

- Bloomfield, D. S., Higgins, P. A., McAteer, R. T. J., & Gallagher, P. T. (2012, Mar). Toward reliable benchmarking of solar flare forecasting methods. *The Astrophysical Journal Letters*, *747*(2), L41.
- Bothmer, V., & Schwenn, R. (1998, January). The structure and origin of magnetic clouds in the solar wind. *Annales Geophysicae*, *16*, 1-24. doi: 10.1007/s00585-997-0001-x
- Burlaga, L., Sittler, E., Mariani, F., & Schwenn, R. (1981, August). Magnetic loop behind an interplanetary shock: Voyager, Helios, and IMP 8 observations. *J. Geophys. Res.*, *86*(A8), 6673-6684. doi: 10.1029/JA086iA08p06673
- Burlaga, L. F. (1988, July). Magnetic clouds and force-free fields with constant alpha. *J. Geophys. Res.*, *93*, 7217-7224. doi: 10.1029/JA093iA07p07217
- Chen, J. (1996, December). Theory of prominence eruption and propagation: Interplanetary consequences. *Journal of Geophysical Research: Space Physics*, *101*(A12), 27499-27519. Retrieved 2016-07-14, from <http://onlinelibrary.wiley.com/doi/10.1029/96JA02644/abstract> doi: 10.1029/96JA02644
- Chen, J., Cargill, P. J., & Palmadesso, P. J. (1997, July). Predicting solar wind structures and their geoeffectiveness. *J. Geophys. Res.*, *102*(A7), 14701-14720. doi: 10.1029/97JA00936
- dos Santos, L. F. G., Narock, A., Nieves-Chinchilla, T., Nuñez, M., & Kirk, M. (2020, October). Identifying Flux Rope Signatures Using a Deep Neural Network. *Sol. Phys.*, *295*(10), 131. doi: 10.1007/s11207-020-01697-x
- Dungey, J. W. (1961, January). Interplanetary Magnetic Field and the Auroral Zones. *Phys. Rev. Lett.*, *6*, 47-48. doi: 10.1103/PhysRevLett.6.47
- Echer, E., Gonzalez, W. D., Tsurutani, B. T., & Gonzalez, A. L. C. (2008, May). Interplanetary conditions causing intense geomagnetic storms (Dst  $\leq$  -100 nT) during solar cycle 23 (1996-2006). *Journal of Geophysical Research (Space Physics)*, *113*(A5), A05221. doi: 10.1029/2007JA012744
- Friedman, J. H. (2001). Greedy function approximation: A gradient boosting machine. *The Annals of Statistics*, *29*(5), 1189-1232.
- Galvin, A. B., Kistler, L. M., Popecki, M. A., Farrugia, C. J., Simunac, K. D. C., Ellis, L., ... Steinfeld, D. (2008). The plasma and suprathermal ion composition (plastic) investigation on the stereo observatories. In C. T. Russell (Ed.), (pp. 437-486). New York, NY: Springer New York.
- Gonzalez, W. D., & Tsurutani, B. T. (1987, September). Criteria of interplanetary parameters causing intense magnetic storms (Dst of less than -100 nT). *Planet. Space Sci.*, *35*, 1101-1109. doi: 10.1016/0032-0633(87)90015-8
- Hanssen, A., & Kuipers, W. (1965). *On the relationship between the fre-*

- quency of rain and various meteorological parameters: (with reference to the problem of objective forecasting). Staatsdrukkerij. Retrieved from <https://books.google.at/books?id=nTZ80gAACAAJ>
- Jin, M., Manchester, W. B., van der Holst, B., Sokolov, I., Tóth, G., Mullinix, R. E., ... Gombosi, T. I. (2017, January). Data-constrained Coronal Mass Ejections in a Global Magnetohydrodynamics Model. *ApJ*, *834*(2), 173. doi: 10.3847/1538-4357/834/2/173
- Kay, C., & Gopalswamy, N. (2018, September). The Effects of Uncertainty in Initial CME Input Parameters on Deflection, Rotation,  $B_z$ , and Arrival Time Predictions. *Journal of Geophysical Research (Space Physics)*, *123*(9), 7220-7240. doi: 10.1029/2018JA025780
- Kilpua, E. K. J., Balogh, A., von Steiger, R., & Liu, Y. D. (2017, Nov). Geoeffective Properties of Solar Transients and Stream Interaction Regions. *Space Sci. Rev.*, *212*, 1271-1314. doi: 10.1007/s11214-017-0411-3
- Kim, R. S., Moon, Y. J., Gopalswamy, N., Park, Y. D., & Kim, Y. H. (2014, April). Two-step forecast of geomagnetic storm using coronal mass ejection and solar wind condition. *Space Weather*, *12*(4), 246-256. doi: 10.1002/2014SW001033
- Lepping, R. P., Acuña, M. H., Burlaga, L. F., Farrell, W. M., Slavin, J. A., Schatten, K. H., ... Worley, E. M. (1995, February). The Wind Magnetic Field Investigation. *Space Sci. Rev.*, *71*, 207-229. doi: 10.1007/BF00751330
- Luhmann, J. G., Curtis, D. W., Schroeder, P., McCauley, J., Lin, R. P., Larson, D. E., ... Gosling, J. T. (2008, April). STEREO IMPACT Investigation Goals, Measurements, and Data Products Overview. *Space Sci. Rev.*, *136*, 117-184. doi: 10.1007/s11214-007-9170-x
- Möstl, C., Amerstorfer, T., Palmerio, E., Isavnin, A., Farrugia, C. J., Lowder, C., ... Boakes, P. D. (2018, Mar). Forward Modeling of Coronal Mass Ejection Flux Ropes in the Inner Heliosphere with 3DCORE. *Space Weather*, *16*(3), 216-229. doi: 10.1002/2017SW001735
- Möstl, C., Isavnin, A., Boakes, P. D., Kilpua, E. K. J., Davies, J. A., Harrison, R. A., ... Zhang, T. L. (2017). Modeling observations of solar coronal mass ejections with heliospheric imagers verified with the heliophysics system observatory. *Space Weather*, *15*(7), 955-970.
- Möstl, C., Weiss, A. J., Bailey, R. L., Reiss, M. A., Amerstorfer, T., Hinterreiter, J., ... Stansby, D. (2020, November). Prediction of the In Situ Coronal Mass Ejection Rate for Solar Cycle 25: Implications for Parker Solar Probe In Situ Observations. *ApJ*, *903*(2), 92. doi: 10.3847/1538-4357/abb9a1
- Mulligan, T., Russell, C. T., & Luhmann, J. G. (1998). Solar cycle evolution of the structure of magnetic clouds in the inner heliosphere. *Geophys. Res. Lett.*, *25*, 2959-2962. doi: 10.1029/98GL01302
- Nguyen, G., Aunai, N., Fontaine, D., Le Pennec, E., Van den Bossche, J., Jeandet, A., ... Regaldo-Saint Blancard, B. (2019, April). Automatic Detection of Interplanetary Coronal Mass Ejections from In Situ Data: A Deep Learning Approach. *ApJ*, *874*(2), 145. doi: 10.3847/1538-4357/ab0d24
- Nieves-Chinchilla, T., Colaninno, R., Vourlidas, A., Szabo, A., Lepping, R. P., Boardsen, S. A., ... Korth, H. (2012, June). Remote and in situ observations of an unusual Earth-directed coronal mass ejection from multiple viewpoints. *Journal of Geophysical Research (Space Physics)*, *117*(A6), A06106. doi: 10.1029/2011JA017243
- Nieves-Chinchilla, T., Linton, M. G., Hidalgo, M. A., & Vourlidas, A. (2018, Jul). Elliptic-cylindrical Analytical Flux Rope Model for Magnetic Clouds. *ApJ*, *861*(2), 139. doi: 10.3847/1538-4357/aac951
- Ogilvie, K. W., Chornay, D. J., Fritzenreiter, R. J., Hunsaker, F., Keller, J., Lobell, J., ... Gergin, E. (1995, February). SWE, A Comprehensive Plasma Instrument for the Wind Spacecraft. *Space Sci. Rev.*, *71*, 55-77. doi: 10.1007/BF00751326

- Owens, M. J. (2018, November). Time-Window Approaches to Space-Weather Forecast Metrics: A Solar Wind Case Study. *Space Weather*, *16*(11), 1847-1861. doi: 10.1029/2018SW002059
- Owens, M. J., Arge, C. N., Spence, H. E., & Pembroke, A. (2005). An event-based approach to validating solar wind speed predictions: High-speed enhancements in the wang-sheeley-arge model. *Journal of Geophysical Research: Space Physics*, *110*(A12), n/a–n/a. (A12105) doi: 10.1029/2005JA011343
- Owens, M. J., & Forsyth, R. J. (2013, December). The Heliospheric Magnetic Field. *Living Reviews in Solar Physics*, *10*(1), 5. doi: 10.12942/lrsp-2013-5
- Owens, M. J., Lockwood, M., & Barnard, L. A. (2017, June). Coronal mass ejections are not coherent magnetohydrodynamic structures. *Nature Scientific Reports*, *7*, 4152. doi: 10.1038/s41598-017-04546-3
- Poedts, S., Lani, A., Scolini, C., Verbeke, C., Wijsen, N., Lapenta, G., . . . Depauw, J. (2020, September). EUropean Heliospheric FORecasting Information Asset 2.0. *Journal of Space Weather and Space Climate*, *10*, 57. doi: 10.1051/swsc/2020055
- Reiss, M. A., Temmer, M., Veronig, A. M., Nikolic, L., Vennerstrom, S., Schoengassner, F., & Hofmeister, S. J. (2016, July). Verification of high-speed solar wind stream forecasts using operational solar wind models. *Space Weather*, *14*(7), 2016SW001390. doi: 10.1002/2016SW001390
- Riley, P., Ben-Nun, M., Linker, J. A., Owens, M. J., & Horbury, T. S. (2017, March). Forecasting the properties of the solar wind using simple pattern recognition. *Space Weather*, *15*(3), 526-540. doi: 10.1002/2016SW001589
- Riley, P., Schatzman, C., Cane, H. V., Richardson, I. G., & Gopalswamy, N. (2006, August). On the Rates of Coronal Mass Ejections: Remote Solar and In Situ Observations. *ApJ*, *647*(1), 648-653. doi: 10.1086/505383
- Rouillard, A. P. (2011, June). Relating white light and in situ observations of coronal mass ejections: A review. *Journal of Atmospheric and Solar-Terrestrial Physics*, *73*(10), 1201–1213. doi: 10.1016/j.jastp.2010.08.015
- Rouillard, A. P., Davies, J. A., Forsyth, R. J., Savani, N. P., Sheeley, N. R., Thernisien, A., . . . Carr, C. M. (2009, Jul). A solar storm observed from the Sun to Venus using the STEREO, Venus Express, and MESSENGER spacecraft. *J. Geophys. Res.*, *114*(A7), A07106. doi: 10.1029/2008JA014034
- Salman, T. M., Lugaz, N., Farrugia, C. J., Winslow, R. M., Galvin, A. B., & Schwadron, N. A. (2018, December). Forecasting Periods of Strong Southward Magnetic Field Following Interplanetary Shocks. *Space Weather*, *16*(12), 2004-2021. doi: 10.1029/2018SW002056
- Savani, N. P., Owens, M. J., Rouillard, A. P., Forsyth, R. J., & Davies, J. A. (2010, May). Observational Evidence of a Coronal Mass Ejection Distortion Directly Attributable to a Structured Solar Wind. *ApJ*, *714*, L128-L132. doi: 10.1088/2041-8205/714/1/L128
- Savani, N. P., Vourlidas, A., Szabo, A., Mays, M. L., Richardson, I. G., Thompson, B. J., . . . Nieves-Chinchilla, T. (2015, June). Predicting the magnetic vectors within coronal mass ejections arriving at Earth: 1. Initial architecture. *Space Weather*, *13*, 374-385. doi: 10.1002/2015SW001171
- Shiota, D., & Kataoka, R. (2016, February). Magnetohydrodynamic simulation of interplanetary propagation of multiple coronal mass ejections with internal magnetic flux rope (SUSANOO-CME). *Space Weather*, *14*, 56-75. doi: 10.1002/2015SW001308
- Telloni, D., Antonucci, E., Bemporad, A., Bianchi, T., Bruno, R., Fineschi, S., . . . Susino, R. (2019, November). Detection of Coronal Mass Ejections at L1 and Forecast of Their Geoeffectiveness. *ApJ*, *885*(2), 120. doi: 10.3847/1538-4357/ab48e9
- Török, T., Downs, C., Linker, J. A., Lionello, R., Titov, V. S., Mikić, Z., . . . Wijaya, J. (2018, Mar). Sun-to-Earth MHD Simulation of the 2000 July 14 “Bastille

- Day” Eruption. *ApJ*, *856*, 75. doi: 10.3847/1538-4357/aab36d
- Tsurutani, B. T., Gonzalez, W. D., Gonzalez, A. L. C., Guarnieri, F. L., Gopalswamy, N., Grande, M., . . . Vasyliunas, V. (2006, July). Corotating solar wind streams and recurrent geomagnetic activity: A review. *Journal of Geophysical Research (Space Physics)*, *111*, A07S01. doi: 10.1029/2005JA011273
- Vourlidas, A. (2014, June). The flux rope nature of coronal mass ejections. *Plasma Physics and Controlled Fusion*, *56*(6), 064001. doi: 10.1088/0741-3335/56/6/064001
- Vourlidas, A., Lynch, B. J., Howard, R. A., & Li, Y. (2013, May). How Many CMEs Have Flux Ropes? Deciphering the Signatures of Shocks, Flux Ropes, and Prominences in Coronagraph Observations of CMEs. *Sol. Phys.*, *284*, 179-201. doi: 10.1007/s11207-012-0084-8
- Vourlidas, A., Patsourakos, S., & Savani, N. P. (2019, July). Predicting the geoeffective properties of coronal mass ejections: current status, open issues and path forward. *Philosophical Transactions of the Royal Society of London Series A*, *377*(2148), 20180096. doi: 10.1098/rsta.2018.0096
- Webb, D. F., & Howard, T. A. (2012, June). Coronal Mass Ejections: Observations. *Living Reviews in Solar Physics*, *9*(1), 3. doi: 10.12942/lrsp-2012-3
- Weiss, A. J., Möstl, C., Amerstorfer, T., Bailey, R. L., Reiss, M. A., Hinterreiter, J., . . . Bauer, M. (2021, January). Analysis of Coronal Mass Ejection Flux Rope Signatures Using 3DCORE and Approximate Bayesian Computation. *ApJS*, *252*(1), 9. doi: 10.3847/1538-4365/abc9bd
- Weiss, A. J., Möstl, C., Davies, E. E., Amerstorfer, T., Bauer, M., Hinterreiter, J., . . . Baumjohann, W. (2021, March). Multi point analysis of coronal mass ejection flux ropes using combined data from Solar Orbiter, BepiColombo and Wind. *arXiv e-prints*, arXiv:2103.16187.
- West, J. L. (2004). The geostorm warning mission: enhanced opportunities based on new technology.
- Wold, A. M., Mays, M. L., Taktakishvili, A., Jian, L. K., Odstrcil, D., & MacNeice, P. (2018, March). Verification of real-time WSA-ENLIL+Cone simulations of CME arrival-time at the CCMC from 2010 to 2016. *Journal of Space Weather and Space Climate*, *8*(27), A17. doi: 10.1051/swsc/2018005
- Wood, B. E., & Howard, R. A. (2009, September). An Empirical Reconstruction of the 2008 April 26 Coronal Mass Ejection. *ApJ*, *702*(2), 901-910. doi: 10.1088/0004-637X/702/2/901
- Zhang, J., Richardson, I. G., Webb, D. F., Gopalswamy, N., Huttunen, E., Kasper, J. C., . . . Zhukov, A. N. (2007, October). Solar and interplanetary sources of major geomagnetic storms ( $Dst \leq -100$  nT) during 1996-2005. *Journal of Geophysical Research (Space Physics)*, *112*(A10), A10102. doi: 10.1029/2007JA012321